Title

Determination of peak ordering in the CrCoNi medium-entropy alloy via nanoindentation

Authors

Zhang, Mingwei

Yu, Qin

Frey, Carolina

et al.

Publication Date

2022-12-01

DOI

10.1016/j.actamat.2022.118380

Acta Materialia 241 (2022) 118380

Contents lists available at ScienceDirect

Acta Materialia

journal homepage: www.elsevier.com/locate/actamat

Full length article

Determination of peak ordering in the CrCoNi medium-entropy alloy via nanoindentation

Mingwei Zhang[a,b], Qin Yu[a,c], Carolina Frey[d], Flynn Walsh[a,c], Madelyn I. Payne[a], Punit Kumar[a,c], Dongye Liu[a], Tresa M. Pollock[d], Mark D. Asta[a,c], Robert O. Ritchie[a,c], Andrew M. Minor[a,b,*]

[a] Department of Materials Science and Engineering, University of California, Berkeley, CA 94720, USA
[b] National Center for Electron Microscopy, Molecular Foundry, Lawrence Berkeley National Laboratory, Berkeley, CA 94720, USA
[c] Materials Sciences Division, Lawrence Berkeley National Laboratory, Berkeley, CA 94720, USA
[d] Materials Department, University of California, Santa Barbara, CA 93106, USA

ARTICLE INFO

Article history:
Received 11 August 2022
Revised 21 September 2022
Accepted 22 September 2022
Available online 25 September 2022

Keywords:
Short-range order
Micro-/nanoindentation
Mechanical properties
Mechanisms
High/medium entropy alloys

ABSTRACT

Local chemical ordering (LCO) in the CrCoNi medium-entropy alloy was investigated by transmission electron microscopy (TEM) after different annealing treatments and their corresponding mechanical properties by bulk tensile tests and nanoindentation. A cold-rolled alloy was annealed at 1000°C for 0.5 h followed by ice water quenching and then aged at a number of different temperatures (600°C, 700°C, 800°C, 900°C, and 1000°C) under vacuum for 240 h to generate different degrees of chemical ordering. A splat-quenched sample rapidly cooled from the liquid phase was also examined. While bulk mechanical properties did not vary among samples with equivalent grain sizes, nanoindentation tests revealed notable differences. As indicated by the load at first pop-in using a Berkovich tip or the indentation yield strength via continuous stiffness measurements using a 10 μm spherical tip, the nanoindentation tests revealed that the stress for onset of plasticity during indentation varied with heat treatment and peaked in the 900°C aged sample. Energy-filtered TEM characterization indicated the presence of ordering in all specimens, with a higher degree of LCO in the aged samples relative to the splat-quenched and 1000°C-quenched samples. The evolution of LCO during aging was determined to occur on the time scale similar to those of bulk diffusion. The difference in nanoindentation strength was attributed to the difference in dislocation nucleation barriers imposed by different degrees of LCO.

1. Introduction

The development of multi-principal element alloys (MPEAs), also referred to as medium- or high-entropy alloys, over the past two decades has yielded structural materials with unprecedented mechanical properties [1–6]. A widely studied example is the FCC single-phase equiatomic CrCoNi ternary alloy that possesses an excellent combination of strength and ductility and the highest fracture toughness reported to date at cryogenic temperatures [7,8], making it an eminent candidate for cryogenic applications such as liquefied gas storage and space exploration. It is believed that these highly desired properties originate from a unique sequence of deformation mechanisms, involving the motion and multiplication of Shockley partial dislocations which result in the formation of stacking faults (SF) that grow into SF parallelepipeds and the nucleation and growth of nanotwins and HCP phases [7,9-15], all of which contribute to continuous strain hardening up to large plastic strains. These mechanisms collectively provide a high degree of sustained strain hardening.

The formation and growth of all these deformation-accommodating defects is closely related to the material's stacking fault energy (SFE), which is in turn governed by the local chemical environment within the crystal. Therefore, extensive research was focused on how concentrated solid solutions may form unique local chemical environments that can strongly affect the mechanical properties of these MPEAs [16–22]. A key finding in these studies is the presence of local chemical order in MPEAs, either in configurations of first/second nearest neighbor short-range order (SRO) or longer ranged forms, due to preferential bonding

* Corresponding Author: Andrew M. Minor, Department of Materials Science and Engineering, University of California, Berkeley, 2607 Hearst Ave. Berkeley, CA 94720, USA, Phone: (510) 495-2749, FAX: (510) 486-5888.
E-mail address: aminor@lbl.gov (A.M. Minor).

https://doi.org/10.1016/j.actamat.2022.118380

of atoms of certain species. The formation of LCO can significantly change the local SFE of the material and influences the nucleation and glide resistance of dislocations, which may influence the deformation mechanisms and mechanical properties of the material. Thus, understanding the nature of LCO and its formation kinetics can in turn enable the tuning of LCO by alloy design and thermomechanical processing routes for better mechanical properties.

Many initial studies on LCO in the Cr-Co-Ni system were based on computation and simulations because the effects of LCO remained elusive under experimental investigations. Tamm *et al.* [23] originally predicted a strong driving force for SRO formation in CrCoNi using density functional theory (DFT)-based Monte Carlo (MC) simulations. Using similar techniques, Ding *et al.* [24] demonstrated how SRO can raise SFEs, which are theoretically negative in random solid solutions due to the metastability of the FCC phase, by up to 90 mJ/m^2, in line with values inferred from the measured dissociation of partial dislocations. While the SFEs of concentrated alloys are inherently complicated to experimentally measure [25,26] and negative SFEs are not fundamentally impossible, these calculations showed how SRO can stabilize the FCC phase and prevent an allotropic phase transition to HCP that is observed in similarly metastable Co and Co-Ni alloys. They concluded that tuning the SRO and therefore the SFE of the material is paramount to developing deformation nanotwins and FCC to HCP phase transformation to enhance the strength and ductility of the alloy. Walsh *et al.* [27] carried out first-principles calculations for a CrCoNi alloy and further argued for the existence of widespread local ordering. In terms of mechanical properties, Jian *et al.* [28] performed hybrid MC/MD simulations on the same alloy and determined that higher degrees of SRO increase the barrier of Shockley partial nucleation and yield strength in an originally dislocation free crystal. Subsequent plasticity was observed to be accommodated by nanotwin nucleation due to the enhanced glide resistance resulting from lattice distortion and SRO at a high MD strain rate of 5×10^8 s^{-1}.

Recently, the direct observation of LCO in CrCoNi has been achieved by energy-filtered transmission electron microscopy (EFTEM). Zhang *et al.* [25] utilized a Zeiss LIBRA TEM that incorporates a monochromator and an in-column Ω filter to characterize LCO in an CrCoNi alloy and discovered increasing streaking in the diffraction pattern on the [110] zone axis for 1000°C, 120 h aged samples. Corresponding dark field (DF) images are associated with features on the order of 1.13±0.43 nm. Chen *et al.* [29] and Zhou *et al.* [26] combined EFTEM, nanobeam diffraction, STEM-HAADF, and atomic resolution EDS techniques to investigate LCO in a VCoNi alloy aged at 900°C for 150 s and a CrCoNi alloy aged at 600°C and 1000°C for 1 h and revealed diffuse 1/2[311] spots in the diffraction pattern on the [112] zone axis. DF and inverse FFT images showed an average LCO feature size of ∼ 0.5 nm, which is the length scale of several nearest-neighbor distances that corresponds to SRO. In addition, enrichment of Cr and (Co, Ni) on alternating {311} planes was observed by EDS mapping, suggesting a (Co, Ni)-Cr type ordering in the FCC lattice. Probability density functions (PDFs) extracted from their EDS line scan were consistent with SRO in CrCoNi featuring unfavored Cr-Cr bonding at the nearest neighbor positions, consistent with previous theoretical predictions.

Despite the success in characterizing LCO in CrCoNi alloys, direct experimental evidence relating LCO to dislocation behaviors and mechanical properties is still scarce, and possible effects of LCO remain largely speculative. Indeed, the exact nature of LCO in CrCoNi-based alloys and its relationship to thermal processing remains somewhat ambiguous. Yin *et al.* [30] suggested limited LCO contribution to the yield strength of bulk CrCoNi by comparing tensile data obtained on samples aged under different conditions. In contrast, Zhang *et al.* [25] conducted nanoindentation experiments and collected the first pop-in loads for CrCoNi in both as-solutionized and 1000°C, 120 h aged forms. Pop-ins are associated with homogeneous or heterogeneous nucleation of dislocations at high stresses close to the theoretical shear stress, or activation of existing (pinned) dislocations at much lower stresses, followed by a burst of strain due to the propagation and multiplication of these dislocations [31,32]. Zhang *et al.* [25] found a notable increase in the stress required for homogeneous dislocation nucleation due to an increasing amount of LCO via aging. Zhao *et al.* [33] reached a similar conclusion for CrCoFeNi and CrCoFeMnNi MPEAs in as-solutionized and 900°C, 24 h aged samples. From the information provided by this limited number of studies, it is argued that nanoindentation may be a more sensitive method to detect certain mechanical effects of LCO. We propose that nanoindentation is sensitive to LCO in a quantitative manner for the following two reasons: (i) LCO is a type of weak obstacle against dislocation glide and it is therefore difficult to separate the contribution of LCO from other parameters, such as initial dislocation density, grain size and texture in bulk mechanical tests, and (ii) nanoindentation probes localized plastic deformation at intrinsic length scales as small as tens of nanometers that potentially contain few to no pre-existing defects such as dislocations, thus enabling the extraction of dislocation-LCO interactions at the “few dislocations” level. Lastly, we note that direct TEM characterization of LCO, albeit important, is a highly specialized and laborious task, and complications arise when drawing quantitative comparisons across samples with different thicknesses, local bending, and exact diffraction conditions. By contrast, nanoindentation is a high-throughput method that can quickly generate a large amount of data to create statistical results. Therefore, mechanical changes associated with ordering phenomena can be assessed across a wide range of heat treatments, as we demonstrate in this work.

In the present study, we report on the nanoindentation results of CrCoNi alloys subjected to various heat treatments: from splat quenching that generates a rapid rate of cooling which would theoretically minimize LCO, to water quenching from the recrystallizing temperature, and further aging at 600-1000°C for 10 days to allow longer periods of time for the formation of order. Mechanical characterization of the alloy with different degrees of LCO involved load measurements at first pop-in as well as yield strengths obtained from indentation stress-strain curves generated by continuous stiffness measurements. A detailed comparison of different samples is generated by a combination of quantitative and statistical analyses of the nanoindentation data and qualitative S/TEM characterization of LCO and deformation microstructure. Bulk mechanical testing was also performed as a baseline and to contrast with the nanoindentation data. Finally, an optimal aging temperature is presented that maximizes the nanoindentation strength of CrCoNi.

2. Experimental

An equiatomic CrCoNi alloy was fabricated by arc-melting high-purity (>99.9%) elements under Ar atmosphere and drop cast into rectangular cross-section copper molds. The casting was then homogenized in vacuum at 1200°C for 24 h and cold rolled to a final thickness of ∼6.1 mm (∼76% reduction in thickness). Full recrystallization of the cold rolled material was achieved by further annealing at 1000°C for 0.5 h followed by ice water quenching. This short annealing time was used to prevent significant grain growth and retain a sufficient number of grains in the specimen cross-section for good polycrystalline behavior in subsequent tensile tests. The material at this stage is labeled as “WQ” in the remainder of this paper. In order to promote different degrees of LCO, several samples were cut, encapsulated in evacuated quartz tubes, and aged at 600°C, 700°C, 800°C, 900°C, or 1000°C for 240 h. After aging, the samples were quickly cooled to room temperature by water

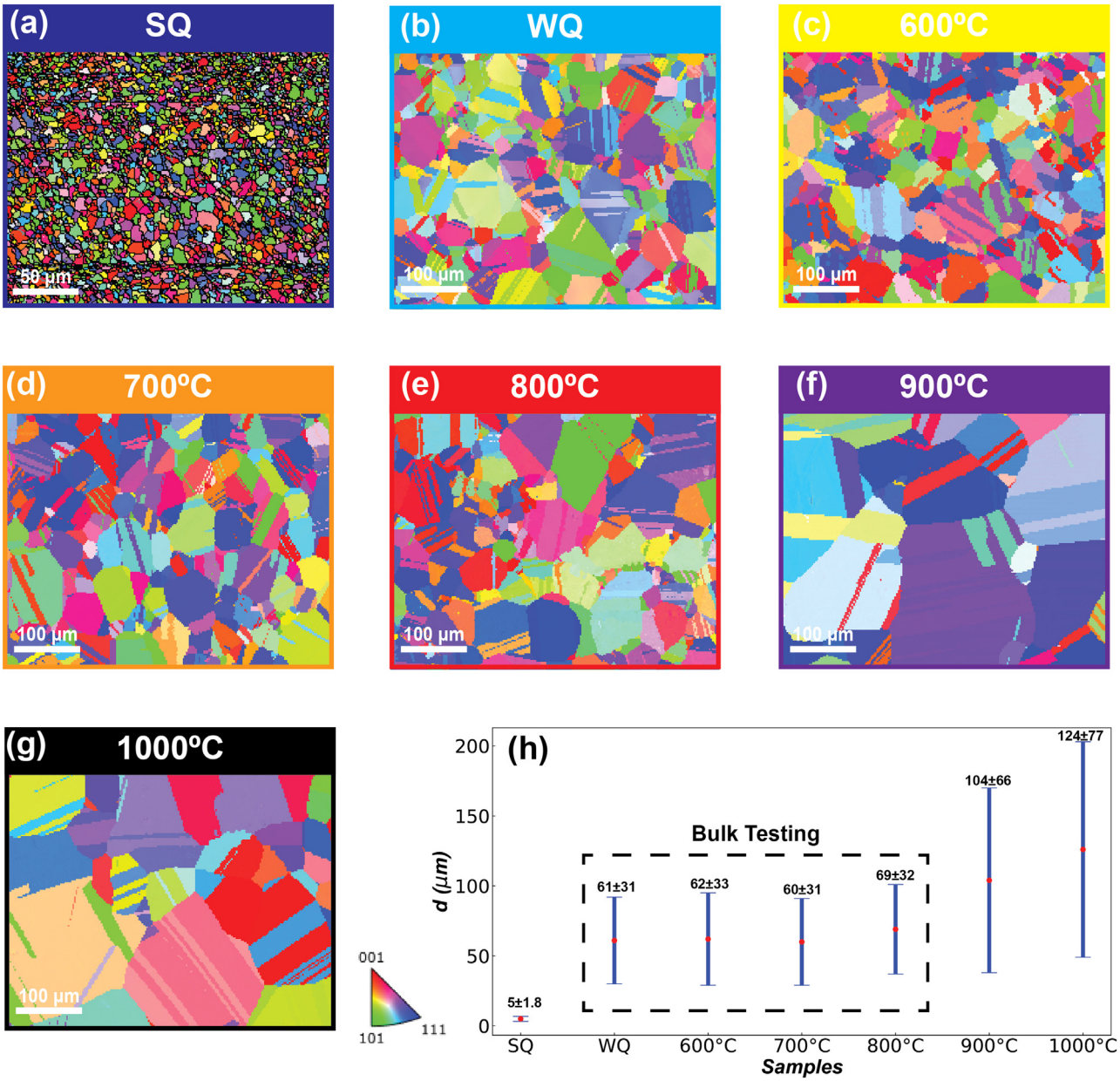

Fig. 1. EBSD inverse pole figure color maps of (a) SQ; (b) WQ; (c) 600°C aged; (d) 700°C aged; (e) 800°C aged; (f) 900°C aged; and (g) 1000°C aged CrCoNi samples. The average grain size, *d*, of these samples and their standard deviations are given in (h). The dashed rectangle highlights the samples selected for bulk mechanical testing due to their similar grain size.

quenching. These samples are labeled by their aging temperatures in the remainder of the paper.

A separate batch of CrCoNi samples was prepared by splat quenching to minimize LCO formation. A modified tri-arc splat quenching system composed of a water-cooled 70 at% Cu-W hearth and a TZM hammer was utilized to rapidly cool a 0.2-0.3 g sample [34]. A Ti getter was inserted to consume excess oxygen in the Ar-filled chamber. The resulting foils are approximately 25.4-31.8 mm in diameter and range in thickness from 50 to 300 µm. These materials are labeled as "SQ" in the remainder of the paper.

Electron backscatter diffraction (EBSD) characterization of the initial microstructure of the heat treated CrCoNi samples was performed on an FEI Scios2 DualBeam FIB SEM using an operating voltage of 20 kV. The EBSD data were post-processed using the AztecCrystal software using a procedure similar to that described in Ref. [35]. The results are shown in Fig. 1, where all samples exhibit an FCC single phase free of second phase formation during heat treatment. The absence of the formation of any long-range ordered compounds is verified by further TEM investigation described in the next section. The high cooling rate that resulted from the splat quenching gives a very fine grain size of 5±1.8 µm. The WQ samples after homogenization at 1000°C for 0.5 h feature an intermediate grain size of ~60±30 µm. Grain growth is limited when the WQ samples were subsequently aged below 900°C. Therefore, only four types of samples, WQ, 600°C, 700°C, and 800°C-aged with near equal grain sizes were selected for comparative bulk tensile testing and Vickers indentation hardness measurements to probe the effect of LCO on the bulk mechanical properties isolated from different contributions of Hall-Petch hardening. Although the Hall-Petch constants for CrCoNi are available to extrapolate samples to equal grain size [36,37], the effect of different LCO cannot be decoupled from the yield strength when these

constants were obtained, thus obscuring the comparison. Dog-bone plate specimens with gauge dimensions of 16 mm × 1.2 mm × 1.2 mm were cut from these materials by electro-discharge machining (EDM) and mechanically polished to grit 800. Uniaxial tensile tests were performed using a 10 kN electro-servo hydraulic 810 MTS load frame operated by an Instron 8800 digital controller. An Epsilon Tech Model 3442 extensometer was used to directly measure the displacement within the gage length. All the tensile testing was performed under a constant engineering strain rate of 1.8×10^{-3} /s. To evaluate reproducibility, three specimens were tensile tested for each heat treatment condition.

Vickers indentation hardness tests were carried out on an Instron 5594 universal testing system using a diamond Vickers indenter. All samples for Vickers indentation testing were mechanically polished down to 1 μm surface finish followed by vibration polish in 0.05-μm SiC particle suspension for at least 6 h. Conforming to ASTM E92-17, the Vickers indentation was conducted by applying an indentation force of 5 kgf (49 N) on the sample surface within 10 s and holding for 10 s before unloading. The two diagonal lengths of the Vickers indent were measured by digital optical microscope and their mean value was used to derive the Vickers hardness following $HV_{(N/mm^2)} = 0.1891 \frac{F_{(N)}}{d_{v\ (mm)}^2}$, where HV is the Vickers hardness, F and d_v are the applied force and mean diagonal length, respectively. d_v was measured to be ~ 0.2 mm for CrCoNi. Ten tests were repeated for each heat treatment condition.

Nanoindentation experiments were conducted on a Bruker TI-950 Triboindenter using a Berkovich tip with a nominal radius of 150 nm to study the effect of LCO on first pop-in loads. In order to account for tip blunting from previous use, the tip radius was calibrated by fitting the elastic loading portion of the indentation data (averaged over a 4×4 indentation grid) on a standard fused quartz sample according to the Hertzian contact theory [38]:

$$P = \frac{4}{3} E_r R^{1/2} h^{3/2}, \tag{1}$$

where P is the indentation load, E_r = 68 GPa [39] is the reduced modulus of the standard fused quartz sample, R is the tip radius, and h is the indentation displacement. The tip radius was determined to be 339±17 nm. All CrCoNi samples were involved in nanoindentation tests because the difference in grain sizes above the micrometer level has a negligible effect on nanoindentation results where the deformation length scale lies well below 1 µm at first pop-in [40,41]. For each sample, 300 nanoindentation tests were carried out across three separate 10×10 square grids of indents with each indent separated from its nearest neighbors by 25 μm. The loading rate and peak load were set to 200 μN/s and 10,000 μN. Note that although all first pop-in loads were below 1,000 μN, a large peak load was chosen to leave clear indents for subsequent EBSD and TEM characterization. The samples were prepared by first mechanically polishing to 1200 grit then electropolishing at −20 °C under a stable current of ~25 mA in an electrolyte consisting of 70% methanol, 20% glycerol, and 10% perchloric acid.

A separate set of nanoindentation data was generated by continuous stiffness measurements (CSM) to obtain indentation stress-strain (ISS) curves using the nanoscale dynamic mechanical analysis (nanoDMA) functionality of the Bruker TI-950 Triboindenter. A diamond spherical indenter with a tip radius of 10 µm was used for a well-defined plastic zone underneath the indenter tip verified by finite element analysis [42] for robust ISS curves. A loading rate of 325 µN/s, an oscillation frequency of 220 Hz, and a peak load of 10,000 µN were used to generate ISS curves to ~5% strain. Since the contact radius measured in CSM measurements is on the order of 1 µm at the top load of 10,000 µN, SQ specimens (d = 5 µm) were not included because of a possible grain size effect. The ISS curves were extracted from the nanoindentation data using the procedures described in Refs. [42–45], where the indentation stress, σ_{ind}, and strain, ε_{ind}, can be written as:

$$\sigma_{ind} = \frac{P}{\pi a^2}, \tag{2}$$

$$\varepsilon_{ind} = \frac{4}{3\pi} \frac{h}{a}, \tag{3}$$

where the contact radius, a, can be directly calculated from the stiffness, S, in CSM tests by $a = \frac{S}{2E_r}$. A total of 40 CSM tests were performed on each sample across four separate 2×5 grids of indents with a separation of 25 µm.

EFTEM was conducted on a Zeiss LIBRA 200MC microscope equipped with an in-column Ω energy filter at an accelerating voltage of 200 kV to directly validate the existence of LCO before nanoindentation. Diffraction patterns were obtained on the [112] zone axis using an energy slit of 5 eV to filter inelastically scattered electrons. The TEM samples used for LCO analysis were cut and thinned by mechanical polishing to 1200 grit followed by twin-jet polishing by a Fischione Model 110 electropolisher using the aforementioned solution and parameters. The dislocation structure formed during nanoindentation was characterized by the diffraction contrast imaging (DCI) technique on an FEI F20 UT Tecnai STEM under an accelerating voltage of 200 kV. The samples used for dislocation analysis were prepared by the FIB-liftout technique on an FEI Scios2 DualBeam FIB SEM under an operating voltage of 30 kV followed by polishing at 5 kV and 2 kV.

3. Results and Discussion

3.1. The Effect of Local Chemical Ordering on Bulk Mechanical Properties

Fig. 2(a) shows representative tensile stress-strain curves for WQ, 600°C, 700°C, and 800°C aged CrCoNi samples, which display a consistent grain size. The curves mostly overlap with no noticeable difference except for some scatter in the elongation to fracture. Fig. 2(b) compares the yield strength, uniform elongation, and UTS extracted from the stress-strain curves as well as Vickers hardness of different samples. Detailed data are also given in Table 1. It can be concluded that any difference among these samples revealed by bulk mechanical testing is marginal, and that LCO developed during heat treatments in this range does not have a noticeable effect on the bulk mechanical properties of the CrCoNi alloy. This invariance of bulk mechanical properties with respect to annealing at 800-1200 ºC is consistent with most literature results, specifically Inoue *et al.* [46] and Refs. [8,12,47-52] compiled by Yin *et al.* [30] who argued that the reported differences in yield strength can be explained by different extents of Hall-Petch hardening and LCO plays no significant role. In addition, when extrapolated to infinite grain size using known Hall-Petch coefficients experimentally measured from samples with different grain sizes [36,37], the yield strength can be satisfactorily estimated by the concentrated solid solution hardening theory proposed by Varvenne *et al.* [16] for random solid solutions. Similarly, Zhou *et al.* [53] reported no difference in the microhardness and yield strength of CrMnFeCoNi single crystals aged from 900-1200°C, even though 1/3[422] diffuse superlattice peaks were observed in the [111] zone axis, indicating the existence of LCO. These bulk mechanical testing results unanimously show that promoting LCO via heat treatment does not have any notable impact on the bulk yield strength.

A rough estimate of the extra strength provided by LCO can be provided by considering the diffuse antiphase boundary (DAPB) energy, γ_{DAPB}, since dislocation slip events destroy LCO and create DAPBs that raise the energy of the crystal. This contribution in a

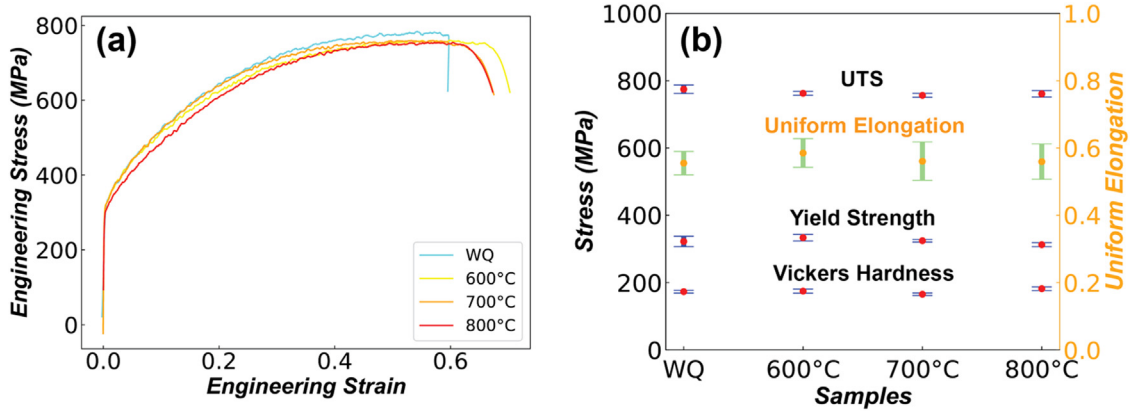

Fig. 2. (a) Representative tensile stress-strain curves of WQ, 600°C, 700°C, and 800°C aged CrCoNi samples.; (b) Yield strengths, uniform elongation, and UTS obtained from the stress-strain curves along with Vickers hardness obtained from microhardness tests. (For interpretation of the references to color in this figure, the reader is referred to the web version of this article.)

Table 1
Vickers hardness, tensile yield strength, UTS, and uniform elongation of WQ, 600°C, 700°C, and 800°C aged CrCoNi samples.

Material	Vickers Hardness (MPa)	Yield Strength (MPa)	UTS (MPa)	Uniform Elongation
WQ	173.3±4.1	321±15	774±11	0.55±0.03
600°C aged	174.8±6.2	331±10	763±3	0.59±0.04
700°C aged	165.5±3.8	323±3	757±4	0.56±0.06
800°C aged	182.1±5.4	312±5	761±10	0.56±0.05

bulk sample can be calculated by [54]:

$$\Delta\sigma_{SRO} = 0.81M\frac{\gamma_{DAPB}}{2b}\left(\frac{3\pi f}{8}\right)^{\frac{1}{2}}, \quad (4)$$

where $M = 3.06$ is the Taylor factor of an untextured FCC crystal, and f is the volume fraction of the LCO clusters. Since γ_{DAPB} is not currently available for the CrCoNi alloy, a γ_{DAPB} of ~25 mJ/m^2 in Ni-10%Al and $Co_{30}Fe_{16.67}Ni_{36.67}Ti_{16.6}$ alloys computed by recent studies [19,22] was used to perform the estimation. We note that this value is appropriate for LCO-related DAPB energy and should be much lower than that for long-range ordered clusters (e.g. >100 mJ/m^2 in Co- or Ni-based superalloys [55–57]). Assuming a uniform distribution of clusters, a volume fraction f of ~6.7% can be obtained by converting the areal fraction of ~20% and average size of ~0.5 nm measured by Zhou *et al.* [26] via atomic resolution TEM imaging and assuming uniform distribution of these clusters. These numbers give an extra strength of 35 MPa, which is an approximately 10% increase in yield strength compared to a random alloy.

3.2. The Effect of Local Chemical Ordering on Nanomechanical Properties

The scenario changes when CrCoNi is subjected to nanoindentation, where the volume undergoing plastic deformation as well as the number of dislocations present initially in this volume are significantly reduced when compared to the volume probed in a bulk tensile test. A schematic is provided in Fig. 3 to illustrate why bulk tensile and Vickers hardness tests that probe multiple grains failed to provide any meaningful correlation with heat treatment (LCO), whereas nanoindentation tests that only probe a very small volume within one grain can potentially capture the effects of LCO. Fig. 4 shows the first 1000 μN of loading from the indentation load-displacement (P-h) curves using a Berkovich tip, where the first pop-ins are clearly visible as a large burst of displacement with negligible change in load. Detailed statistics of these data can be found in Table 2. It is worth noting that pop-ins in nanoindentation may be analogous to yield drops in tensile tests (at least

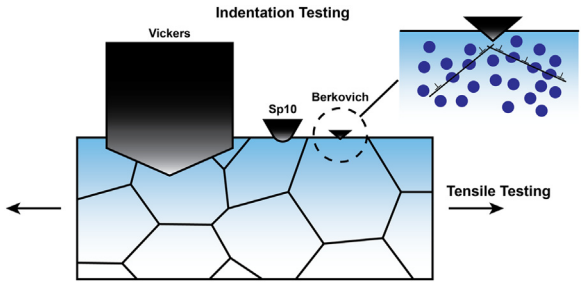

Fig. 3. Schematic of different mechanical testing conditions that probe plastic deformation at different length scales in a CrCoNi alloy. The LCO contributions to mechanical strength can only be meaningfully probed in small deformation volumes by nanoindentation (the Berkovich tip and 10 μm spherical tip, Sp10, used in this study are shown). The LCO clusters are represented by blue circles in the inset.

in cases where the pop-ins are due to activation of pinned dislocations). The magnitude of the yield drop has been associated in some cases with the degree of LCO [58,59], whereas others reported no such correlation [60,61].

The values of first pop-in loads are within the range of those obtained for CrCoNi, CrCoFeNi, and CrCoFeMnNi in other nanoindentation studies using indenter tips of similar radii [25,33,62-64]. A large scatter in those results was observed for all samples, as the first pop-in load can be affected by surface roughness, grain boundaries, interstitial atoms, local dislocation density, and other factors [65–67]. Therefore, the nanoindentation data have to be treated in a statistical manner, with more meaning ascribed to the highest pop-in loads since they are probing the intrinsic nanomechanical properties of the crystals, as compared to the lowest values which can be explained by extrinsic factors such as those described above. Fig. 4(h) gives the cumulative probability distribution of the first pop-in loads, where a clear increasing trend in the order SQ-WQ-600°C-700°C-1000C-800°C-900°C can be observed for higher loads (e.g., above the median value where $F = 0.5$). As expected, significant overlap exists at lower loads ($F <$

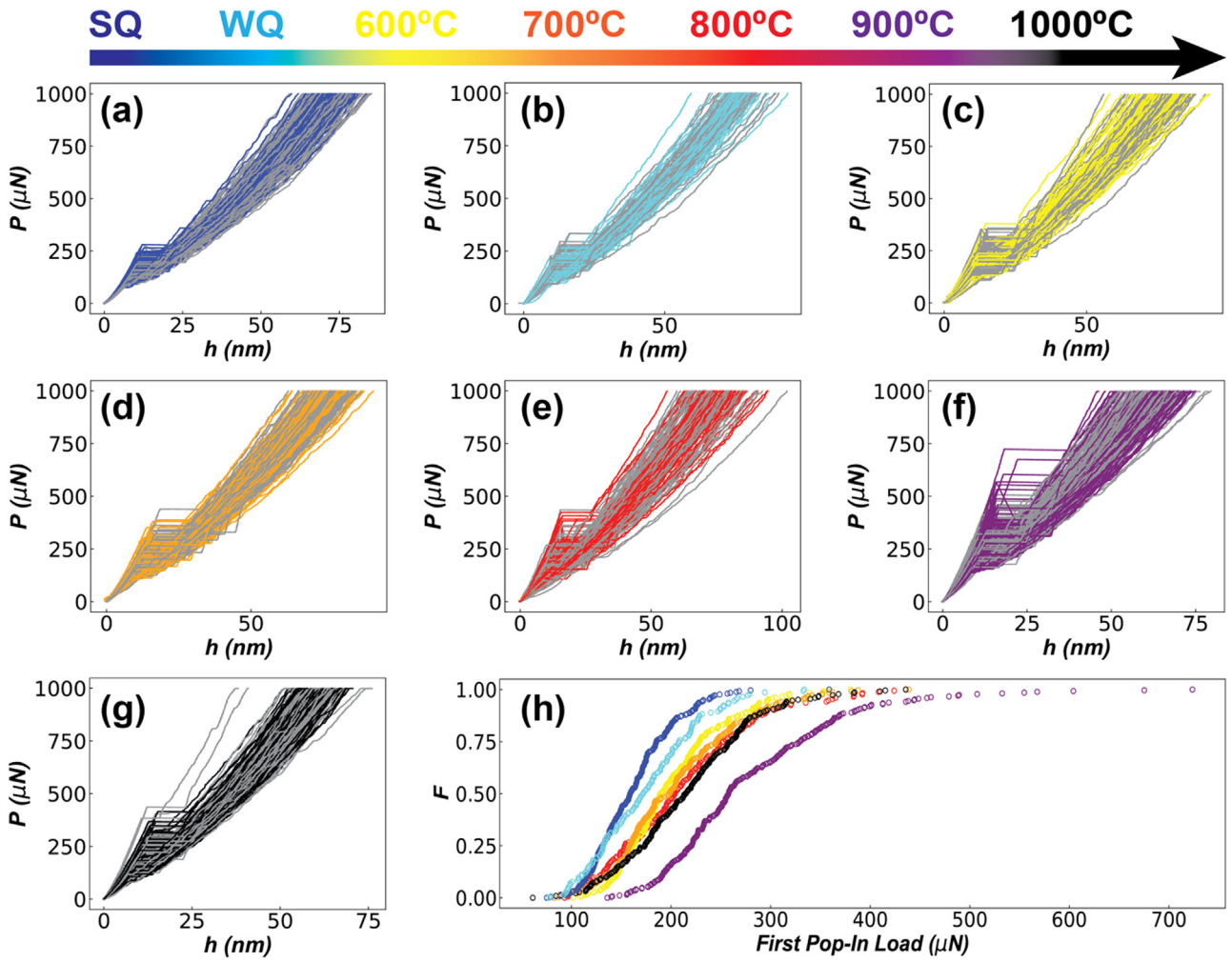

Fig. 4. Nanoindentation load-displacement curves for (a) SQ; (b) WQ; (c) 600°C; (d) 700°C; (e) 800°C; (f) 900°C; and (g) 1000°C aged CrCoNi samples using a Berkovich tip. The cumulative probability distribution of first pop-in loads, F, is given in (h). The gray curves in figures (a)-(g) serve merely as a visual guide for easy recognition of the pop-in loads. (For interpretation of the references to color in this figure, the reader is referred to the web version of this article.)

Table 2
Statistical results for first pop-in loads and the activation volumes of the SQ, WQ, 600°C, 700°C, and 800°C, 900°C, and 1000°C aged CrCoNi samples.

Material	Avg. First Pop-in Load (μN)	Min. First Pop-in Load (μN)	Max. First Pop-in Load (μN)	$V^*(b^3)$
SQ	163.5±41.2	75.2	358.8	0.56±0.01
WQ	174.4±52.7	77.2	333.8	0.42±0.01
600°C aged	201.0±52.8	101.8	380.3	0.54±0.01
700°C aged	204.3±63.1	82.6	438.7	0.44±0.01
800°C aged	211.3±72.4	93.2	435.7	0.38±0.01
900°C aged	279.5±89.4	135.9	723.6	0.42±0.01
1000°C aged	216.3±65.9	61.1	435.7	0.43±0.01

0.25), since these indents are likely affected by local defects (e.g., grain boundaries, dislocations, surface steps) so that the unlocking of pre-existing dislocations or heterogeneous nucleation of dislocations dominate, yielding a significantly lower pop-in load. Therefore, these indents are of less interest because the effect of LCO cannot be distinguished from other controlling factors.

The effect of crystallographic orientation was examined to ensure a fair comparison across indents located in different grains. Fig. 5 gives a representative overlay of the EBSD inverse pole figure (IPF) color map showing the grain morphology and a 10×10 nanoindentation grid on a 700°C aged sample. The first pop-in loads that correspond to these indents are visualized on the right figure as a pixelated color map. The black pixels (zero pop-in load) depict indents that did not experience a pop-in. The values appear to disperse randomly and no correlation of first pop-in loads with grain orientation was observed. This result is typical of all samples tested and is consistent with the findings in similar FCC MPEAs [33,64].

The cumulative distribution function, F, can be further utilized to compute the activation volume for the rate-determining event that controls plasticity. Mason *et al.* [40] laid out the first-order analytical solution for incipient plasticity during nanoindentation based on the nucleation of at least one dislocation under a shear stress of τ. The activation volume, V^*, can be written as:

$$V^* = \frac{\pi}{0.47}\left(\frac{3R}{4E_r}\right)^{2/3} kT \cdot \alpha, \tag{5}$$

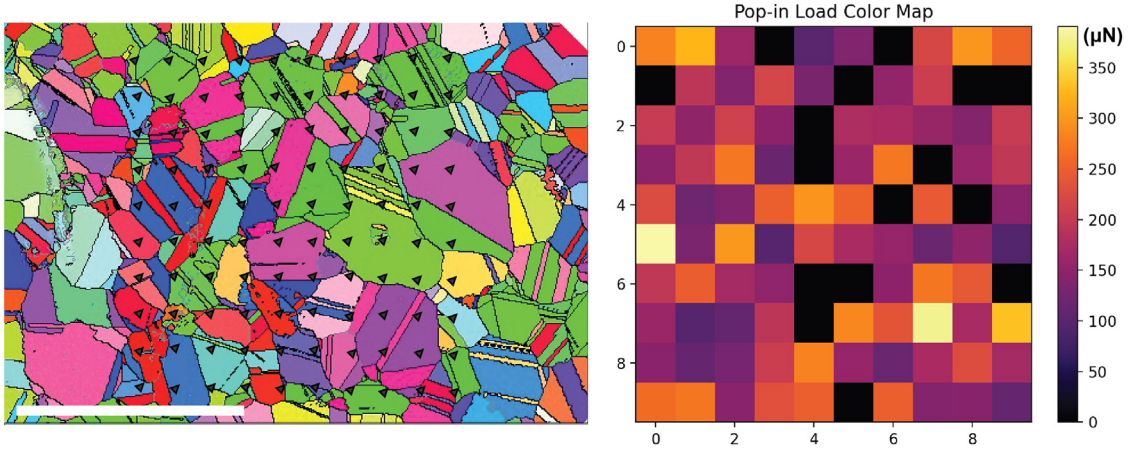

Fig. 5. EBSD IPF color map showing a representative visualization of a 10×10 nanoindentation grid on a 700°C aged sample. The scale bar in the figure indicates 200 μm. The visualization is typical for all samples despite the difference in grain size. The size of the indents was exaggerated for better visibility. The corresponding color map for first pop-in loads is shown on the right, where the black pixels (zero first pop-in load) delineate indents for which pop-ins were not observed. The numbers in the x- and y-axis of the map indicate the coordinates of the indent. (For interpretation of the references to color in this figure, the reader is referred to the web version of this article.)

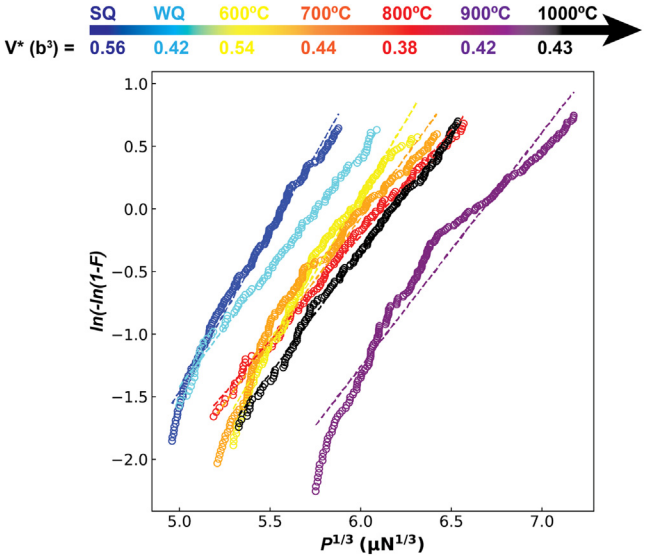

Fig. 6. Plot of $ln(-ln(1-F))$ versus $P^{1/3}$ plot that was used to extract the activation volume of plasticity under nanoindentation for SQ, WQ, 600°C, 700°C, 800°C, 900°C, and 1000°C aged CrCoNi samples. The tails of the data that could contain outliers were omitted and only the data within the range of the mean value plus/minus one standard deviation were selected for linear regression. The activation volumes were measured to be $\sim 0.5b^3$, as marked above the plot. (For interpretation of the references to color in this figure, the reader is referred to the web version of this article.)

where k is Boltzmann constant, T is the absolute temperature, and α is the slope of the line obtained from linear regression of $ln(-ln(1-F))$ against $P^{1/3}$. Fig. 6 provides the plot of $ln(-ln(1-F))$ versus $P^{1/3}$ plot with the V^* values computed by Eq. 5 also given; these values and their respective standard deviations are also compiled in Table 2. The values of $ln(-ln(1-F))$ were truncated such that only those within the range of the mean value plus/minus one standard deviation were considered; this was done to preclude less reliable data at the tails of the distribution, as suggested by Mason *et al.* [40]. A universal V^* of $\sim 0.5b^3$ was determined for all samples, which indicates a single deformation mechanism. This value is consistent with that measured for dislocation nucleation mechanisms [40,68], including those obtained for CrCoNi-based FCC MPEAs that suggest homogeneous nucleation or heterogeneous nucleation at monovacancies [33].

Deeper insights into the deformation mechanisms can be drawn by analyzing the distribution of the shear stress at yield (or pop-in), τ_y, from nanoindentation data, which can be calculated by:

$$\tau_y = 0.31\left(\frac{6E_r}{\pi^3 R^2}P\right)^{1/3}. \quad (6)$$

Here we follow the method used in by Zhao *et al.* [33] to describe the distribution of τ_y by the kernel density estimation (KDE). Zhao *et al.* reported little difference in using the Gaussian distribution or the log-normal dislocation as the kernel, and thus the Gaussian distribution is selected here for simplicity. The Gaussian KDE of τ_y is given in Fig. 7(a), which evidently shows a large scatter in data as well as overlapping τ_y at the low stress end that repeat the findings from the cumulative probability distribution in Fig. 4(h). The average value of τ_y is shown on the plot as a dashed vertical line. Even though roughly the same trend is observed as that in Fig. 4(h), the difference in the average values is much smaller than the scatter and therefore is statistically insignificant. A closer look at the KDE may lead to using a bimodal distribution to describe the τ_y values, as shoulders are clearly visible within the curves. This observation agrees with the Gaussian KDE curves in Zhao *et al.* [33], where they deconvoluted the curves into two Gaussian peaks that represent homogeneous nucleation and heterogeneous nucleation of dislocations. Such treatment, although reasonable, is not applied in our study because the wide distribution of pop-in loads suggests most nucleation is heterogeneous to some extent, leading to a distribution of τ_y values. Since the selection of fitting parameters (e.g., the bandwidth of the Gaussian kernels) for the KDE and the initial guess of the location of the peaks is subjective, the average τ_y values extracted can be largely biased. Here, the difference in τ_y among differently aged samples is qualitatively presented by τ_y data that are greater than one standard deviation above the mean value for each sample. Two criteria formed the basis for selecting these data: (i) a high τ_y that corresponds to a low initial defect density is desired because as discussed above, it highlights the role played by LCO in a more "pristine" crystal compared to deformation mechanisms dominated by pre-existing defects; (ii) the need for enough data points for the analysis to remain statistically sound. The resulting Gaussian KDE is shown in Fig. 7(b), which shows significantly reduced scatter and a clearer separation of average τ_y across different samples. The increasing τ_y in the order SQ-WQ-600°C-700°C-1000°C-800°C-900°C is robustly repeated. Admittedly, the selection of the cutoff is arbitrary and only used to better demonstrate the trend, and such cutoff is not used in the

Table 3
Statistical results for τ_y from nanoindentation *P-h* curves using a Berkovich tip (both for all data and for selected data greater than one standard deviation above the mean) and $\sigma_{ind,y}$ from ISS curves using a 10 μm spherical tip for SQ, WQ, 600°C, 700°C, and 800°C, 900°C, and 1000°C aged CrCoNi samples.

Material	Avg. τ_y (GPa)	Min. τ_y (GPa)	Max. τ_y (GPa)	Avg. τ_y for selected data (GPa)	Avg. $\sigma_{ind,y}$ from CSM with pop-in (GPa)	Avg. $\sigma_{ind,y}$ from CSM without pop-in (GPa)
SQ	7.08±0.59	5.51	9.28	8.11±0.28	–	–
WQ	7.22±0.74	5.56	9.06	8.45±0.26	2.60±0.46	1.61±0.27
600°C aged	7.59±0.65	6.10	9.46	8.77±0.26	3.41±1.04	2.18±0.64
700°C aged	7.61±0.79	5.69	9.92	9.01±0.31	3.53±0.86	2.00±0.36
800°C aged	7.68±0.88	5.92	9.90	9.33±0.33	3.85±1.07	1.86±0.33
900°C aged	8.46±0.85	6.72	11.73	10.19±0.57	5.34±1.87	2.29±0.45
1000°C aged	7.76±0.81	5.14	9.90	9.18±0.32	3.47±0.75	2.30±0.49

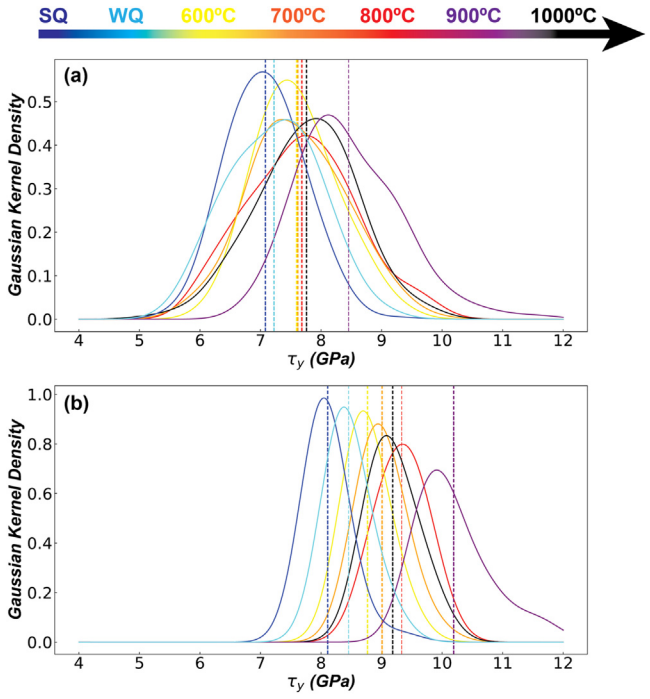

Fig. 7. (a) Gaussian kernel density estimation of shear stress at first pop-in events, τ_y, for SQ, WQ, 600°C, 700°C, 800°C, 900°C, and 1000°C aged CrCoNi samples; and (b) the same estimation using only the data with values greater than one standard deviation above the mean value. The average value of τ_y for each sample is delineated by a dashed vertical line. (For interpretation of the references to color in this figure, the reader is referred to the web version of this article.)

upcoming analyses. Detailed data presented in Fig. 7 are also given in Table 3. Reminiscent of the fact that the activation volume measured for all samples is consistent, which suggests a single mechanism, the difference in τ_y can most likely be attributed to the difference in LCO resulting from different heat treatment conditions. Specifically, a maximum of the degree of LCO is identified at 900°C. The peaking of LCO determined at such a high temperature is indeed intriguing, as ordering is thermodynamically favorable at lower temperatures (e.g., 600°C in our case), and kinetics is hardly believed to be limiting for Angstrom-level SRO formation. This result is discussed in detail in **Section 3.4.2**. The average τ_y for the selected data is in the range of ~8-10 GPa, which is on the order of G/10, where G~90 GPa is the shear modulus of CrCoNi [69]. This value is close to the theoretical shear strength of the crystal, which is appropriate for the mechanism of homogeneous nucleation of Shockley partials as suggested by previous experimental and MD studies on FCC crystals, including MPEAs [28,33,40,70]. In addition, CrCoNi produces a higher τ_y than its counterparts CrCoFeNi and CrMnFeCoNi [33,64], which may or may not be ascribed to increasing LCO because CrCoNi is generally stronger due to a higher shear modulus, a larger misfit volume, and a higher extent of solid-solution hardening [8,71]. However, it is important to see that the promotion of local ordering in CrCoNi can cause an increase up to ~20% in τ_y under nanoindentation, which is quite significant as compared to the bulk behavior.

In order to further support these findings, continuous stiffness measurements (CSM) were performed to generate indentation stress-strain (ISS) curves that serve as a different way to describe the yield behavior during nanoindentation. High reliability of the ISS curves was maintained by using a relatively large spherical tip (10 μm in radius) with a well-defined plastic zone [42]. Therefore, the results from CSM cannot be directly compared to those obtained from the Berkovich measurements due to the indentation size effect [72]. Zhao *et al.* [33] used spherical indenters with radii of 0.5 μm and 12.7 μm to test CrCoFeNi and CrMnFeCoNi HEAs and found a significantly lower yield strength for the larger tip. This behavior is attributed to a higher probability of encountering pre-existing defects for larger tips that create a larger deformation volume [31]. Hence, our aim was to utilize CSM to provide a qualitative validation for the previous Berkovich nanoindentation results by reproducing the observed trend of first pop-in loads for the aged samples. Representative ISS curves with yield strengths close to the average value for each type of specimen are shown in Fig. 8. The curves can be divided into two categories: those that do (Fig. 8(a)) or do not (Fig. 8(b)) show apparent pop-ins featured by a significantly higher yield strength followed by a large strain burst and load drop that correspond to dislocation nucleation and propagation. Detailed values for indentation yield strengths are provided in Table 3. The average yield strengths are much lower than those obtained with a Berkovich tip and compare favorably with the values in Zhao *et al.* [33] using a 12.7 μm tip, showing a strong indentation size effect. The trend observed in previous nanoindentation tests was indeed confirmed by ISS curves that show large pop-ins, and the clear maximum at 900°C was again captured. The difference in yield strengths obtained from ISS curves without obvious pop-ins, however, is more subtle, which resembles the low stress end in Fig. 4(h) and Fig. 7(a). Therefore, the results from the two separate set of nanoindentation experiments are largely consistent.

3.3. (S)TEM Characterization of LCO and Nanoindentation Deformation Microstructure

The nanoindentation data shown above evidently reveal the differences in the nanomechanical properties of CrCoNi that are caused by different degrees of chemical order developed during various heat-treatment conditions. To support this hypothesis, we characterized the LCO in CrCoNi samples before nanoindentation and examined the deformation microstructure after nanoindentation to provide qualitative evidence via electron microscopy. To compare the most different microstructures, we selected the SQ and WQ samples, along with the 900°C-aged that exhibited maximum nanoindentation yield strength, as well as one sample aged above this temperature, at 1000°C, and one below, at 800°C, for

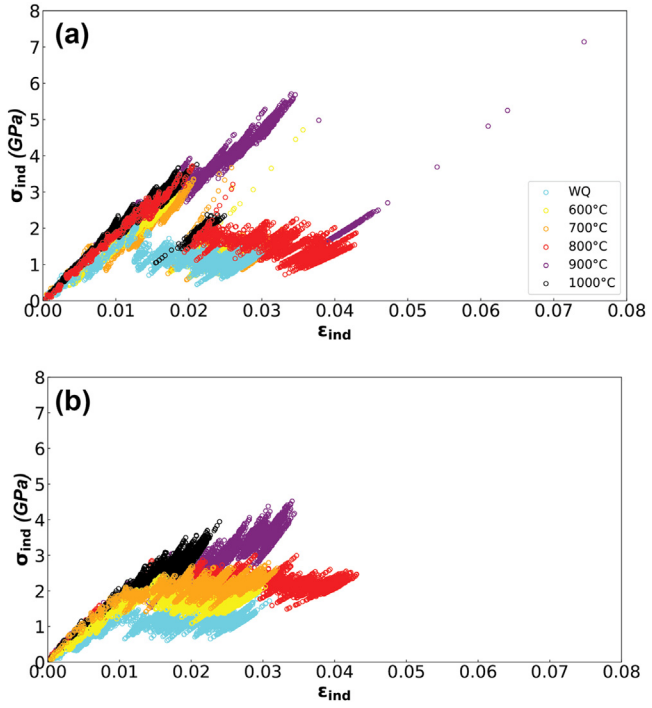

Fig. 8. Representative indentation stress-strain curves obtained from continuous stiffness measurements using a spherical diamond tip of 10 μm in radius. The curves can be separated into two categories: (a) those where initial pop-ins were observed or (b) not observed. (For interpretation of the references to color in this figure, the reader is referred to the web version of this article.)

(S)TEM analysis. Fig. 9 shows the diffraction pattern from EFTEM characterization of a 900°C aged sample on the [112] zone axis, where diffuse superlattice peaks at 1/2[311] positions are clearly visible, suggesting the same type of LCO reported by Zhou *et al.* [26]. This feature is representative in diffraction patterns of all selected samples, and the line profiles provided below show two distinct peaks at these positions, including in the SQ and WQ samples, as shown in Fig. 9(c). The profiles were normalized by the sum of the intensity of the image to allow for a qualitative comparison of peak intensities in samples with different thicknesses (all samples were determined to be 70-90 nm thick by the EELS log-ratio technique). It should be reiterated that the peak intensities cannot be compared quantitatively due to slight differences in thickness, diffraction condition, sample preparation, among other extrinsic factors. For example, one cannot conclude that the lower peak intensity of the 800°C aged sample than 900°C means that the 800°C aged sample has a lower fraction of LCO clusters because it might merely be a sample effect. However, three important conclusions can be drawn with confidence: (i) LCO exists in all of the selected samples, even including the SQ sample that experienced the fastest cooling rate examined, which is proven by the universal presence of diffuse 1/2[311] superlattices despite a difference in intensities. *This means that the comparison generated throughout the paper is based on different degrees of LCO instead of LCO versus a random solid solution.* This finding provides further rationale for the similar bulk mechanical properties obtained above.; (ii) no long-range order was observed after aging as no sharp superlattice peaks were apparent. This evidence indicates the absence of the nucleation and growth of intermetallic precipitates; (iii) there is a 100-fold increase in the intensity of diffuse 1/2[311] superlattice peaks for aged samples compared to SQ and WQ samples that cannot be solely attributed to sample effects, suggesting growth of the LCO domains during aging. It should be emphasized that such growth does not involve a change in the spatial frequency of compositional fluctuations, as the reciprocal vectors for LCO remain at 1/2[311] positions. In other words, if the compositional fluctuation is interpreted as concentration waves as suggested by Ding *et al.* [73], the wavelength along the direction perpendicular to the {311} planes remains unchanged, and the increase in the superlattice peak intensity after aging may also reflect an increase in

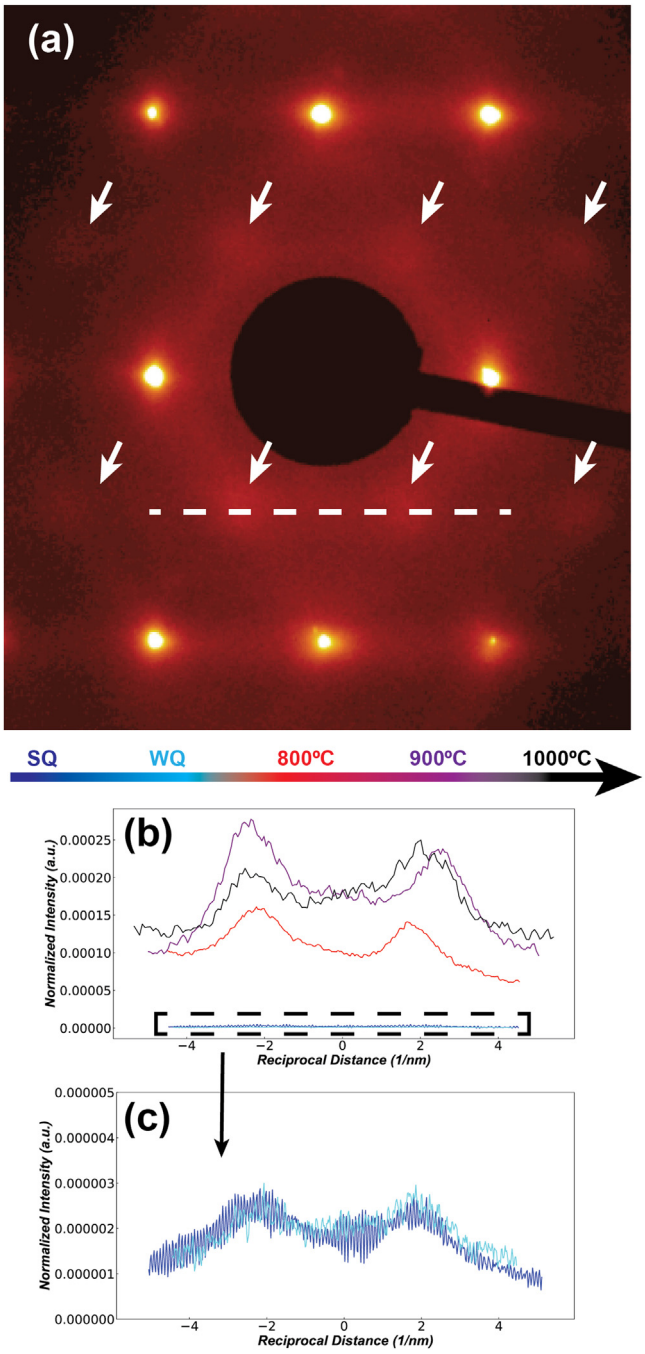

Fig. 9. (a) Representative EFTEM diffraction pattern of a 900°C aged CrCoNi sample before nanoindentation on [112] zone axis, where the diffuse 1/2[311] superlattice peaks that suggest LCO are marked by the arrows. The diffraction pattern was color coded to enhance visibility. The line profiles of the intensity of these superlattice peaks are shown in (b) for SQ, WQ, 800°C, 900°C, and 1000°C aged samples. The intensities were normalized by the sum of the intensity of the image to compare among different samples and therefore are in arbitrary units. The dashed box highlights the line profiles of SQ and WQ specimens, and their expanded view is provided in (c) due to their low intensities. The existence of the same superlattice peaks is confirmed. (For interpretation of the references to color in this figure, the reader is referred to the web version of this article.)

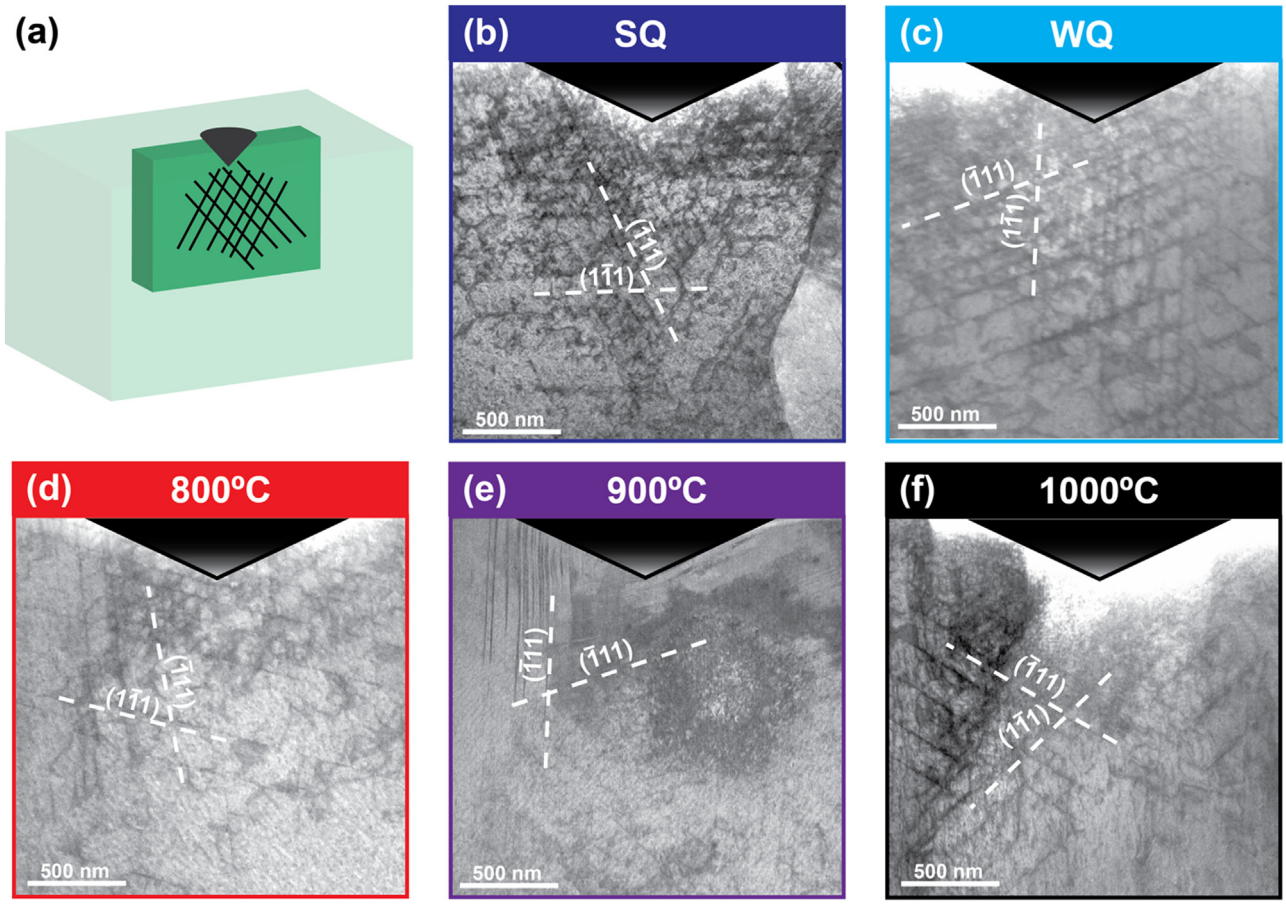

Fig. 10. (a) Schematic of the FIB-liftout sample geometry that was used for nanoindentation; and DCI-STEM images that show the deformation microstructure of (b) SQ; (c) WQ; (d) 800°C; (e) 900°C; and (f) 1000°C aged samples after nanoindentation. The black triangles in the STEM images indicate the location of the indent.

the wave amplitude. Further discussion on the spatial and compositional evolution of LCO during aging is given in the next section.

Characterization of the deformation microstructure underneath the indents is given in Fig. 10. The deformation mode was determined to be the planar slip of dislocations along two {111} planes for all selected samples, which is consistent with the characteristic slip mode when LCO is present and causes glide plane softening [25,74]. The common deformation mode, along with a universal activation volume of $\sim 0.5b^3$ in all samples, combined with direct characterization of LCO provided above, supports the fact that the difference in nanoindentation yield strength can be directly attributed to the difference in the degrees of LCO without the occurrence of any change in deformation mechanisms. As a result, the LCO strengthening of the CrCoNi MPEA on the nanoscale is an intrinsic effect.

3.4. Discussion of Experimental Results

3.4.1. Peak LCO Formation from Nanoindentation Results

The main results of this paper can be summarized into a diagram for LCO formation that provides a direct connection between aging temperatures and the mechanical properties governed by LCO, as shown in Fig. 11. This is somewhat analogous to a Time-Temperature-Transformation "TTT" diagram except that we have only probed one time value at a given temperature and it is not clear if LCO formation is always the same with a well-defined composition and phase fraction, although extracting the areal fraction of LCO using advanced (S)TEM tools has been shown to be possible [25,26,29]. Nonetheless, a mechanical representation instead of phase formation percent is perhaps more meaningful in that it directly reflects the properties desired for alloy design and optimization. The pseudo-TTT diagrams based on the shear strength measured at the first pop-in events and continuous stiffness measurement (CSM) yield strength are given in Fig. 11(a) and (b), respectively. The selection of data only at the high stress end for first pop-ins conducted in Fig. 7(b) was not repeated here to reflect the overall statistics without any subjectivity in data interpretation. The apparent nose at 900°C points out the optimal temperature to age CrCoNi for maximum LCO development as a tradeoff of thermodynamic and kinetic driving forces.

3.4.2. The Evolution of LCO during Aging

It is paramount to understand the evolution of LCO during aging and its implications on the mechanical properties. Specifically, three elements of this evolution: the nature of the LCO, the time scale, and the length scale of LCO formation and growth are of interest. Like most FCC alloys containing Cr as a principal element, CrCoNi exhibits a first-order phase transition in the vicinity of 700 ºC that is reminiscent of the formation of $CrNi_2$ in the binary Cr-Ni system [75]. In a separate study, Inoue *et al.* suggested the ordered phase appears to involve $L1_2$ ordering of Cr using spatial distribution maps of elements in their correlative TEM and atom probe tomography (APT) analysis [46]. Interestingly, $CrNi_2$ has a $MoPt_2$-type crystal structure that will result in Cr segregation in every third {311} plane, whereas atomic EDS measurements performed by Zhou *et al.* [26] found Cr segregation in every other {311} plane, rendering a CrNi motif that is metastable and unfamiliar in the FCC families. Although the exact nature of LCO in CrCoNi remains elu-

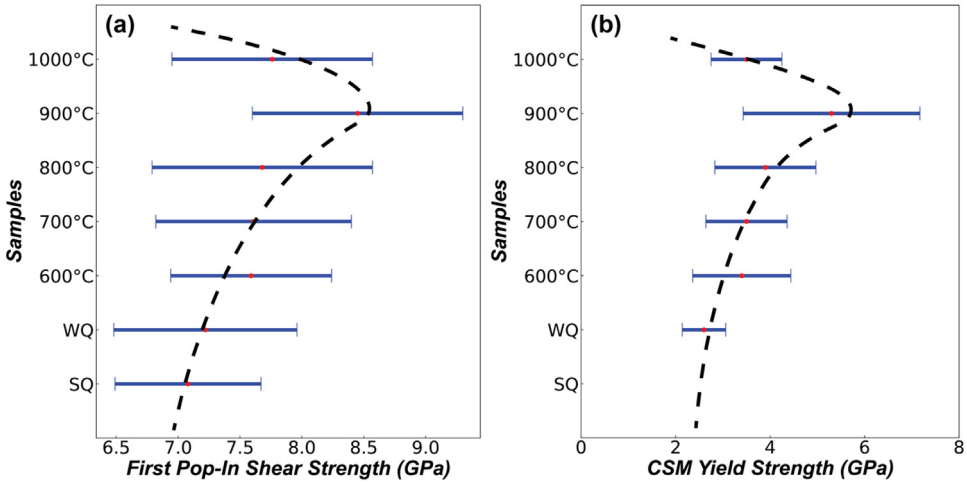

Fig. 11. Pseudo-TTT diagrams of the LCO evolved under different heat treatment conditions using (a) first pop-in shear strength; and (b) CSM yield strength as mechanical representations. The dashed curves serve as a visual guide to the eye.

sive, two important conclusions can be made according to our experimental results and the above discussion of other studies: (i) The complete formation of any Cr-containing intermetallic compound with long-range order in CrCoNi via the conventional nucleation and growth mechanism during aging is absent because no sharp superlattice peaks were observed. Therefore, the enhancement of the LCO is a compositionally continuous process; and (ii) such enhancement is verified by the intensity increase in the diffuse 1/2[311] superlattice peaks and the difference in nanoindentation results.

It is interesting to discuss the time scale and length scale of LCO formation and growth. If LCO in CrCoNi is limited to first/second nearest neighbor SRO and barring the existence of a novel ordered structure in CrCoNi, higher temperature SRO should reach its equilibrium extent rather quickly. One can roughly estimate the relevant time scale according to the theory of Cook [76] for regular FCC solutions, where the equilibration time:

$$\tau = \frac{a^2}{32D} \cdot \frac{T + 3T_c}{T - T_c}, \tag{7}$$

can be determined for lattice constant $a = 3.56$ Å and the diffusivity $D = D_0 \exp(-Q/kT)$, where the pre-exponential factor, $D_0 = 3.5 \times 10^{-3}$ m^2/s and the activation energy $Q = 3.42$ eV as determined by Jin *et al.* [77]. Taking $T_c = 950$ K [75], at 800 ºC, 900 ºC, and 1000 ºC, τ respectively equals 0.4 s, 0.01 s, and 0.0005 s. These times are consistent with kinetic Monte Carlo simulations of a model MPEA system, which suggest that SRO forms over sub-second time scales [78]. Indeed, indications of ordering in WQ and even SQ samples are observed in the present study, indicating that SRO can form even at the very high cooling rate experienced during splat quenching. Similar degrees of ordering were also observed in samples quenched from 600 ºC and 1000 ºC in another study [26]. In the present study, all samples except for SQ have been homogenized at 1000 ºC for 0.5 h after cold rolling, which is a much longer time frame than sub-seconds, in which nearest-neighbor SRO forms. It is therefore intriguing, for example, why aging for 240 h at 1000 ºC produces different mechanical and TEM diffraction results as compared to WQ samples that were aged for 0.5 h at the same temperature. It is thus reasonable to propose that the growth of LCO is likely to take place at length and time scales much larger than that for nearest neighbor SRO, and that longer term annealing increases the intensity of ½[311] peaks due to the stoichiometric incompatibility of this ordering wave with equiatomic CrCoNi. If the intensity increase of the diffuse 1/2[311] superlattice peaks after aging is caused by further Cr enrichment at every other {311} plane, such rearrangement will require longer range Cr transport via bulk diffusion that can take place over a longer time frame ~240 h, in which case kinetics does become limiting. Dark-field images of aged samples in previous studies show clusters larger than those in quenched samples [25,26], indicating spatial growth of ordered clusters during aging. It is likely that the observed nose of mechanical strength after aging at 900 ºC is related to this long-range process, that is, 900 ºC is a balanced thermodynamic and kinetic optimum for LCO growth, instead of formation. In addition, LCO growth can even be accompanied by local phase decomposition, and it can be argued that a continuous phase decomposition that resembles spinodal decomposition may exist in the CrCoNi system, which fits well with the observed time scale and length scale of a possible transformation. Since this paper is focused on the effect of LCO on the mechanical properties, exact microscopic verification of the SRO evolution is beyond the scope of the current study. Still, our observations invite speculation as to the long-term phase stability of the equiatomic CrCoNi alloy at these temperatures and the possible presence of a novel ordered phase. For instance, Zhou *et al.* [53] reported the retarded formation of a seemingly coherent Cr-rich precipitate in {111} planes in CrMnFeCoNi, which is not inconsistent with the observed ordering wave. This may be related to the formation of a sigma phase, which exists in the Cr-Co-Ni system, although is not expected to be favored at the equimolar composition [79].

Regardless of the exact nature, ordering at various length scales could provide an explanation for the apparent distribution of dislocation nucleation barriers, as determined from the first pop-in loads and CSM yield strengths. Combining DFT and MD simulations, Cao *et al.* [80] identified certain Cr-rich localities as the primary source of dislocations. They found unstable BCC-like atomic environments that served as a precursor for dislocation nucleation due to weak Cr-Cr bonding in an FCC lattice. As these motifs are reduced by LCO, they showed that a significant increase in the system's ideal shear strength is achieved when LCO is introduced to a random solid solution. In a similar manner, depleting Cr from other regions could have the same effect, if to a slightly lesser extent. Despite the lack of a measurable effect on bulk yield strength, the possible effects of LCO on strain hardening, HCP and twin formation, and strain hardening remains an important research topic.

4. Conclusions

The current paper provides a detailed investigation of the effect of LCO on the mechanical properties of a CrCoNi alloy that was subjected to various heat treatment conditions, including splat quenching (SQ), and 1000 ºC, 0.5 h homogenization followed by ice water quenching (WQ) and further aging at 600 ºC, 700 ºC, 800 ºC, 900 ºC, and 1000 ºC for 240 h. Based on the results from bulk mechanical testing, nanoindentation, and (S)TEM characterization, the main findings are summarized below:

1 A certain degree of LCO is present in all samples, even in the splat quenched samples that experienced high cooling rates, as shown by the universal appearance of diffuse 1/2[311] superlattice peaks in EFTEM diffraction patterns under the [112] zone axis. However, long-range order is absent in all samples. This finding suggests that any LCO-related difference in the mechanical properties is only caused by the difference in its degree. The intensity of diffuse 1/2[311] superlattice peaks significantly increases after aging, which signifies growth of LCO clusters in bulk diffusion time frame.
2 Bulk tensile testing and Vickers hardness testing show no significant effects from SRO on WQ, 600 ºC, 700 ºC, and 800 ºC aged samples that have similar grain sizes. This finding indicates that the effect of aging (LCO) on the dislocation glide resistance in CrCoNi is negligible. The lack of variation in these results may also be explained by the presence of certain LCO in the WQ sample.
3 The first pop-in stress (measured by nanoindentation with a Berkovich tip) increases in the following order: SQ-WQ-600 ºC-700 ºC-1000 ºC-800 ºC-900 ºC aged samples. The same trend was observed in the yield strengths obtained by continuous stiffness measurement using a 10 μm spherical indenter. This increase is attributed to the fact that LCO increases the barrier for dislocation nucleation and initial strain bursts in a crystal with low to zero initial dislocation density. 900 ºC was determined to be the peak aging condition to promote LCO and enhance the nanomechanical properties.

Declaration of Competing Interest

The authors declare that they have no known competing financial interests or personal relationships that could have appeared to influence the work reported in this paper.

Acknowledgements

This work was primarily supported by the U.S. Department of Energy, Office of Science, Basic Energy Sciences, Materials Sciences and Engineering Division, through the Damage-Tolerance in Structural Materials program (KC13) at the Lawrence Berkeley National Laboratory (LBNL) under contract no. DE-AC02-CH11231 (sample preparation, mechanical testing and electron microscopy characterization). Work at the Molecular Foundry was supported by the Office of Science, Office of Basic Energy Sciences, of the U.S. Department of Energy under Contract No. DE-AC02-05CH11231 (electron microscopy facilities). The authors also acknowledge the Schmidt Family Foundation (Grant SB180156) and ONR grant N00014-181-2392 (sample preparation), and Deryck Stave and Chris Torbet for their modifications to the tri-arc system. In addition, helpful discussions with Easo P. George are heartfully acknowledged.

References

[1] J.W. Yeh, S.K. Chen, S.J. Lin, J.Y. Gan, T.S. Chin, T.T. Shun, C.H. Tsau, S.Y. Chang, Nanostructured high-entropy alloys with multiple principal elements: Novel alloy design concepts and outcomes, Adv Eng Mater 6 (5) (2004) 299–303.
[2] B. Cantor, I.T.H. Chang, P. Knight, A.J.B. Vincent, Microstructural development in equiatomic multicomponent alloys, Materials Science and Engineering: A 375-377 (2004) 213–218.
[3] B. Gludovatz, A. Hohenwarter, D. Catoor, E.H. Chang, E.P. George, R.O. Ritchie, A fracture-resistant high-entropy alloy for cryogenic applications, Science 345 (6201) (2014) 1153–1158.
[4] Z. Li, K.G. Pradeep, Y. Deng, D. Raabe, C.C. Tasan, Metastable high-entropy dual-phase alloys overcome the strength-ductility trade-off, Nature 534 (7606) (2016) 227–230.
[5] D.B. Miracle, O.N. Senkov, A critical review of high entropy alloys and related concepts, Acta Mater 122 (2017) 448–511.
[6] E.P. George, W.A. Curtin, C.C. Tasan, High entropy alloys: A focused review of mechanical properties and deformation mechanisms, Acta Mater 188 (2020) 435–474.
[7] B. Gludovatz, A. Hohenwarter, K.V. Thurston, H. Bei, Z. Wu, E.P. George, R.O. Ritchie, Exceptional damage-tolerance of a medium-entropy alloy CrCoNi at cryogenic temperatures, Nat Commun 7 (2016) 10602.
[8] G. Laplanche, A. Kostka, C. Reinhart, J. Hunfeld, G. Eggeler, E.P. George, Reasons for the superior mechanical properties of medium-entropy CrCoNi compared to high-entropy CrMnFeCoNi, Acta Mater 128 (2017) 292–303.
[9] Z. Zhang, M.M. Mao, J. Wang, B. Gludovatz, Z. Zhang, S.X. Mao, E.P. George, Q. Yu, R.O. Ritchie, Nanoscale origins of the damage tolerance of the high-entropy alloy CrMnFeCoNi, Nat Commun 6 (1) (2015) 10143.
[10] Z. Zhang, H. Sheng, Z. Wang, B. Gludovatz, Z. Zhang, E.P. George, Q. Yu, S.X. Mao, R.O. Ritchie, Dislocation mechanisms and 3D twin architectures generate exceptional strength-ductility-toughness combination in CrCoNi medium-entropy alloy, Nat Commun 8 (2017) 14390.
[11] Q. Ding, X. Fu, D. Chen, H. Bei, B. Gludovatz, J. Li, Z. Zhang, E.P. George, Q. Yu, T. Zhu, R.O. Ritchie, Real-time nanoscale observation of deformation mechanisms in CrCoNi-based medium- to high-entropy alloys at cryogenic temperatures, Mater Today 25 (2019) 21–27.
[12] C.E. Slone, S. Chakraborty, J. Miao, E.P. George, M.J. Mills, S.R. Niezgoda, Influence of deformation induced nanoscale twinning and FCC-HCP transformation on hardening and texture development in medium-entropy CrCoNi alloy, Acta Mater 158 (2018) 38–52.
[13] Y. Chen, D. Chen, X. An, Y. Zhang, Z. Zhou, S. Lu, P. Munroe, S. Zhang, X. Liao, T. Zhu, Z. Xie, Unraveling dual phase transformations in a CrCoNi medium-entropy alloy, Acta Mater 215 (2021) 117112.
[14] M. Heczko, V. Mazánová, C.E. Slone, M. Shih, E.P. George, M. Ghazisaeidi, J. Polák, M.J. Mills, Role of deformation twinning in fatigue of CrCoNi medium-entropy alloy at room temperature, Scripta Mater 202 (2021) 113985.
[15] L. Ding, A. Hilhorst, H. Idrissi, P.J. Jacques, Potential TRIP/TWIP coupled effects in equiatomic CrCoNi medium-entropy alloy, Acta Mater 234 (2022) 118049.
[16] C. Varvenne, A. Luque, W.A. Curtin, Theory of strengthening in fcc high entropy alloys, Acta Mater 118 (2016) 164–176.
[17] W.G. Nöhring, W.A. Curtin, Cross-slip of long dislocations in FCC solid solutions, Acta Mater 158 (2018) 95–117.
[18] S. Chen, Z.H. Aitken, S. Pattamatta, Z. Wu, Z.G. Yu, D.J. Srolovitz, P.K. Liaw, Y.-W. Zhang, Simultaneously enhancing the ultimate strength and ductility of high-entropy alloys via short-range ordering, Nat Commun 12 (1) (2021) 4953.
[19] E. Antillon, C. Woodward, S.I. Rao, B. Akdim, T.A. Parthasarathy, Chemical short range order strengthening in a model FCC high entropy alloy, Acta Mater 190 (2020) 29–42.
[20] E. Ma, X. Wu, Tailoring heterogeneities in high-entropy alloys to promote strength–ductility synergy, Nat Commun 10 (1) (2019) 5623.
[21] Q.-J. Li, H. Sheng, E. Ma, Strengthening in multi-principal element alloys with local-chemical-order roughened dislocation pathways, Nat Commun 10 (1) (2019) 3563.
[22] A. Abu-Odeh, M. Asta, Modeling the effect of short-range order on cross-slip in an FCC solid solution, Acta Mater 226 (2022) 117615.
[23] A. Tamm, A. Aabloo, M. Klintenberg, M. Stocks, A. Caro, Atomic-scale properties of Ni-based FCC ternary, and quaternary alloys, Acta Mater 99 (2015) 307–312.
[24] J. Ding, Q. Yu, M. Asta, R.O. Ritchie, Tunable stacking fault energies by tailoring local chemical order in CrCoNi medium-entropy alloys, PNAS 115 (36) (2018) 8919.
[25] R. Zhang, S. Zhao, J. Ding, Y. Chong, T. Jia, C. Ophus, M. Asta, R.O. Ritchie, A.M. Minor, Short-range order and its impact on the CrCoNi medium-entropy alloy, Nature 581 (7808) (2020) 283–287.
[26] L. Zhou, Q. Wang, J. Wang, X. Chen, P. Jiang, H. Zhou, F. Yuan, X. Wu, Z. Cheng, E. Ma, Atomic-scale evidence of chemical short-range order in CrCoNi medium-entropy alloy, Acta Mater 224 (2022) 117490.
[27] F. Walsh, M. Asta, R.O. Ritchie, Magnetically driven short-range order can explain anomalous measurements in CrCoNi, PNAS 118 (13) (2021) e2020540118.
[28] W.-R. Jian, Z. Xie, S. Xu, Y. Su, X. Yao, I.J. Beyerlein, Effects of lattice distortion and chemical short-range order on the mechanisms of deformation in medium entropy alloy CoCrNi, Acta Mater 199 (2020) 352–369.
[29] X. Chen, Q. Wang, Z. Cheng, M. Zhu, H. Zhou, P. Jiang, L. Zhou, Q. Xue, F. Yuan, J. Zhu, X. Wu, E. Ma, Direct observation of chemical short-range order in a medium-entropy alloy, Nature 592 (7856) (2021) 712–716.
[30] B. Yin, S. Yoshida, N. Tsuji, W.A. Curtin, Yield strength and misfit volumes of NiCoCr and implications for short-range-order, Nat Commun 11 (1) (2020) 2507.
[31] S. Shim, H. Bei, E.P. George, G.M. Pharr, A different type of indentation size effect, Scripta Mater 59 (10) (2008) 1095–1098.

[32] H. Bei, Y.F. Gao, S. Shim, E.P. George, G.M. Pharr, Strength differences arising from homogeneous versus heterogeneous dislocation nucleation, Phys Rev B 77 (6) (2008) 060103.
[33] Y. Zhao, J.-M. Park, J.-i. Jang, U. Ramamurty, Bimodality of incipient plastic strength in face-centered cubic high-entropy alloys, Acta Mater 202 (2021) 124–134.
[34] C. Frey, R. Silverstein, T.M. Pollock, A high stability B2-containing refractory multi-principal element alloy, Acta Mater 229 (2022) 117767.
[35] S.E. Broyles, M. Zhang, J.C. Gibeling, Influence of annealing on the creep behavior of GlidCop Al-15, Mater Sci Eng A 779 (2020) 139112.
[36] W. Lu, X. Luo, Y. Yang, B. Huang, Hall-petch relationship and heterogeneous strength of CrCoNi medium-entropy alloy, Mater Chem Phys 251 (2020) 123073.
[37] G.W. Hu, L.C. Zeng, H. Du, X.W. Liu, Y. Wu, P. Gong, Z.T. Fan, Q. Hu, E.P. George, Tailoring grain growth and solid solution strengthening of single-phase CrCoNi medium-entropy alloys by solute selection, J Mater Sci Technol 54 (2020) 196–205.
[38] K.L. Johnson, Contact Mechanics, Cambridge University Press, Cambridge, 1985.
[39] W.C. Oliver, G.M. Pharr, An improved technique for determining hardness and elastic modulus using load and displacement sensing indentation experiments, J Mater Res 7 (6) (1992) 1564–1583.
[40] J.K. Mason, A.C. Lund, C.A. Schuh, Determining the activation energy and volume for the onset of plasticity during nanoindentation, Phys Rev B 73 (5) (2006) 054102.
[41] J.R. Morris, H. Bei, G.M. Pharr, E.P. George, Size Effects and Stochastic Behavior of Nanoindentation Pop In, Phys Rev Lett 106 (16) (2011) 165502.
[42] B.R. Donohue, A. Ambrus, S.R. Kalidindi, Critical evaluation of the indentation data analyses methods for the extraction of isotropic uniaxial mechanical properties using finite element models, Acta Mater 60 (9) (2012) 3943–3952.
[43] S.J. Vachhani, S.R. Kalidindi, Grain-scale measurement of slip resistances in aluminum polycrystals using spherical nanoindentation, Acta Mater 90 (2015) 27–36.
[44] S. Pathak, S.R. Kalidindi, Spherical nanoindentation stress–strain curves, Mater Sci Eng R Rep 91 (2015) 1–36.
[45] S.J. Vachhani, R.D. Doherty, S.R. Kalidindi, Studies of grain boundary regions in deformed polycrystalline aluminum using spherical nanoindentation, Int J Plast 81 (2016) 87–101.
[46] K. Inoue, S. Yoshida, N. Tsuji, Direct observation of local chemical ordering in a few nanometer range in CoCrNi medium-entropy alloy by atom probe tomography and its impact on mechanical properties, Phy Rev Mater 5 (8) (2021) 085007.
[47] Z. Wu, H. Bei, G.M. Pharr, E.P. George, Temperature dependence of the mechanical properties of equiatomic solid solution alloys with face-centered cubic crystal structures, Acta Mater 81 (2014) 428–441.
[48] S. Yoshida, T. Bhattacharjee, Y. Bai, N. Tsuji, Friction stress and Hall-Petch relationship in CoCrNi equi-atomic medium entropy alloy processed by severe plastic deformation and subsequent annealing, Scripta Mater 134 (2017) 33–36.
[49] J. Miao, C.E. Slone, T.M. Smith, C. Niu, H. Bei, M. Ghazisaeidi, G.M. Pharr, M.J. Mills, The evolution of the deformation substructure in a Ni-Co-Cr equiatomic solid solution alloy, Acta Mater 132 (2017) 35–48.
[50] Y.L. Zhao, T. Yang, Y. Tong, J. Wang, J.H. Luan, Z.B. Jiao, D. Chen, Y. Yang, A. Hu, C.T. Liu, J.J. Kai, Heterogeneous precipitation behavior and stacking-fault-mediated deformation in a CoCrNi-based medium-entropy alloy, Acta Mater 138 (2017) 72–82.
[51] S. Praveen, J.W. Bae, P. Asghari-Rad, J.M. Park, H.S. Kim, Ultra-high tensile strength nanocrystalline CoCrNi equi-atomic medium entropy alloy processed by high-pressure torsion, Mater Sci Eng A 735 (2018) 394–397.
[52] S.S. Sohn, A. Kwiatkowski da Silva, Y. Ikeda, F. Körmann, W. Lu, W.S. Choi, B. Gault, D. Ponge, J. Neugebauer, D. Raabe, Ultrastrong medium-entropy single-phase alloys designed via severe lattice distortion, Adv Mater 31 (8) (2019) 1807142.
[53] D. Zhou, Z. Chen, K. Ehara, K. Nitsu, K. Tanaka, H. Inui, Effects of annealing on hardness, yield strength and dislocation structure in single crystals of the equiatomic Cr-Mn-Fe-Co-Ni high entropy alloy, Scripta Mater 191 (2021) 173–178.
[54] A.J. Ardell, Precipitation hardening, Metall Trans A 16 (12) (1985) 2131–2165.
[55] D. Baither, C. Rentenberger, H.P. Karnthaler, E. Nembach, Three alternative experimental methods to determine the antiphase-boundary energies of the γ' precipitates in superalloys, Philos Mag A 82 (9) (2002) 1795–1805.
[56] J.E. Saal, C. Wolverton, Energetics of antiphase boundaries in γ' Co3(Al,W)-based superalloys, Acta Mater 103 (2016) 57–62.
[57] J. Miao, C. Slone, S. Dasari, M. Ghazisaeidi, R. Banerjee, E.P. George, M.J. Mills, Ordering effects on deformation substructures and strain hardening behavior of a CrCoNi based medium entropy alloy, Acta Mater 210 (2021) 116829.
[58] J.B. Cohen, M.E. Fine, Some aspects of short-range order, J. Phys. Radium 23 (10) (1962) 749–762.
[59] R.O. Scattbrgood, M.B. Bever, The relation of short-range order to the deformation behaviour of copper-rich copper-aluminium alloys, Philos Mag A 22 (177) (1970) 501–514.
[60] N. Büttner, E. Nembach, On short-range order hardening in Cu-10 at.% Au, Acta Metall 30 (1) (1982) 83–86.
[61] J. Svitak, R. Asimow, Solid-solution strengthening in the Ag-Au system, Trans Metall Soc AIME 245 (2) (1969) 209–212.
[62] S. Mridha, M. Sadeghilaridjani, S. Mukherjee, Activation volume and energy for dislocation nucleation in multi-principal element alloys, Metals 9 (2) (2019) 263.
[63] J. Yan, W. Fang, J. Huang, J. Zhang, R. Chang, X. Zhang, B. Liu, J. Feng, F. Yin, Plastic deformation mechanism of CoCrxNi medium entropy alloys, Mater Sci Eng A 814 (2021) 141181.
[64] C. Zhu, Z.P. Lu, T.G. Nieh, Incipient plasticity and dislocation nucleation of FeCoCrNiMn high-entropy alloy, Acta Mater 61 (8) (2013) 2993–3001.
[65] S. Pathak, J.L. Riesterer, S.R. Kalidindi, J. Michler, Understanding pop-ins in spherical nanoindentation, Appl Phys Lett 105 (16) (2014) 161913.
[66] F. Pöhl, Pop-in behavior and elastic-to-plastic transition of polycrystalline pure iron during sharp nanoindentation, Sci Rep 9 (1) (2019) 15350.
[67] Y. Gao, H. Bei, Strength statistics of single crystals and metallic glasses under small stressed volumes, Prog Mater Sci 82 (2016) 118–150.
[68] C.A. Schuh, J.K. Mason, A.C. Lund, Quantitative insight into dislocation nucleation from high-temperature nanoindentation experiments, Nat Mater 4 (8) (2005) 617–621.
[69] G. Laplanche, M. Schneider, F. Scholz, J. Frenzel, G. Eggeler, J. Schreuer, Processing of a single-crystalline CrCoNi medium-entropy alloy and evolution of its thermal expansion and elastic stiffness coefficients with temperature, Scripta Mater 177 (2020) 44–48.
[70] H.Y. Liang, C.H. Woo, H. Huang, A.H.W. Ngan, T.X. Yu, Dislocation nucleation in the initial stage during nanoindentation, Philos Mag 83 (31-34) (2003) 3609–3622.
[71] G. Laplanche, P. Gadaud, C. Bärsch, K. Demtröder, C. Reinhart, J. Schreuer, E.P. George, Elastic moduli and thermal expansion coefficients of medium-entropy subsystems of the CrMnFeCoNi high-entropy alloy, J Alloy Compd 746 (2018) 244–255.
[72] G.M. Pharr, E.G. Herbert, Y. Gao, The indentation size effect: a critical examination of experimental observations and mechanistic interpretations, Annu Rev Mater Res 40 (1) (2010) 271–292.
[73] Q. Ding, Y. Zhang, X. Chen, X. Fu, D. Chen, S. Chen, L. Gu, F. Wei, H. Bei, Y. Gao, M. Wen, J. Li, Z. Zhang, T. Zhu, R.O. Ritchie, Q. Yu, Tuning element distribution, structure and properties by composition in high-entropy alloys, Nature 574 (7777) (2019) 223–227.
[74] R. Zhang, S. Zhao, C. Ophus, Y. Deng, S.J. Vachhani, B. Ozdol, R. Traylor, K.C. Bustillo, J.W. Morris, D.C. Chrzan, M.D. Asta, A.M. Minor, Direct imaging of short-range order and its impact on deformation in Ti-6Al, Science Advances 5 (12) (2020) eaax2799.
[75] K. Jin, S. Mu, K. An, W.D. Porter, G.D. Samolyuk, G.M. Stocks, H. Bei, Thermophysical properties of Ni-containing single-phase concentrated solid solution alloys, Mater Des 117 (2017) 185–192.
[76] H.E. Cook, The kinetics of clustering and short-range order in stable solid solutions, J Phys Chem Solids 30 (10) (1969) 2427–2437.
[77] K. Jin, C. Zhang, F. Zhang, H. Bei, Influence of compositional complexity on interdiffusion in Ni-containing concentrated solid-solution alloys, Mater Res Lett 6 (5) (2018) 293–299.
[78] Z. Shen, J.-P. Du, S. Shinzato, Y. Sato, P. Yu, S. Ogata, Kinetic Monte Carlo simulation framework for chemical short-range order formation kinetics in a multi-principal-element alloy, Comp Mater Sci 198 (2021) 110670.
[79] T. Omori, J. Sato, K. Shinagawa, I. Ohnuma, K. Oikawa, R. Kainuma, K. Ishida, Experimental Determination of Phase Equilibria in the Co-Cr-Ni System, J Ph Equilibria Diffus 35 (2) (2014) 178–185.
[80] F.-H. Cao, Y.-J. Wang, L.-H. Dai, Novel atomic-scale mechanism of incipient plasticity in a chemically complex CrCoNi medium-entropy alloy associated with inhomogeneity in local chemical environment, Acta Mater 194 (2020) 283–294.